

# 1 Constructing physical-based rainfall landslides prediction model: 2 Insights from rainfall threshold curves database of slope units

3 Kai Wang<sup>1\*</sup>, Linmao Xie<sup>1</sup>, Shuailong Xie<sup>1</sup>, Shaojie Zhang<sup>2\*</sup>, Yongyang Jiang<sup>3</sup>, Ji Zhang<sup>4</sup>, Lin Zhu<sup>1</sup>, Zhiliu Wang<sup>1</sup>,  
4 Fuzhou Qi<sup>1</sup>

5 *1. School of architecture and civil engineering, Zhongyuan University of Technology, Zhengzhou, 450007, China*

6 *2. Key Laboratory of Mountain Hazards and Earth Surface Process, Institute of Mountain Hazards and  
7 Environment, Chinese Academy of Sciences, Chengdu, 610041, China*

8 *3. Zhejiang Zhongnan Construction Group Steel Structure Co., Ltd, Hangzhou, 311400, China*

9 *4. Sichuan Institution of Geological Engineering Investigation Group Co.LTD, Chengdu, 610041, China*

10 **Abstract:** The commonly used rainfall threshold warning method relies heavily on historical  
11 rainfall and landslide inventory data, which limits its applicability in regions that lack these data.  
12 While physical methods do not rely on landslide inventories to establish warning criteria, the  
13 calculation of the safety factor typically requires considerable time. To address these issues, this  
14 study integrates physical methods, rainfall threshold warning methods, and slope units to develop  
15 a rapid forecasting model for rainfall landslides at a regional scale. A hydrological analysis  
16 technique for slope units based on grid cells was developed to calculate the instability probability  
17 of slope units. Then, each slope unit was analyzed under 20 levels of antecedent effective  
18 precipitation and nearly 200 combinations of rainfall intensity (I) and duration (D) to derive the  
19 key fitting parameters  $\alpha$  and  $\beta$  of the I-D curves under various rainfall scenarios. The application  
20 results from Fengjie County indicate that the model runs in less than 12 min, with missing alarm  
21 and false alarm rates of 11.8% and 21.1%, respectively, highlighting its excellent potential for  
22 practical application. This study is expected to provide insights for the rapid forecasting of rainfall  
23 landslides in the impoverished mountainous regions of developing countries.

24  
25  
26 **Key words:** Landslide forecasting model, Slope unit, Fitting parameters, Warning database

---

\* Corresponding Authors 1: Kai Wang

E-mail: [6696@zut.edu.cn](mailto:6696@zut.edu.cn)

\* Corresponding Authors 2: Shaojie Zhang

E-mail: [sj-zhang@imde.ac.cn](mailto:sj-zhang@imde.ac.cn)

# 1    **1    Introduction**

2        Rainfall-induced landslides at a regional scale are among the most common types of natural  
3    hazards worldwide. Reports indicate that in the United States, rainfall-triggered landslides and  
4    secondary hazards result in 25–50 fatalities and economic losses of approximately \$2 billion  
5    annually (He et al., 2016). This loss is even more severe in developing countries in the Third  
6    World (Wang et al., 2024; Wang et al., 2021; Wang et al., 2023). In recent years, numerous studies  
7    have indicated that regional landslide forecasting is highly effective for hazard prevention and  
8    mitigation. Researchers have developed various rainfall landslide forecasting models based on  
9    statistical and physical methods (Aristizábal et al., 2016; Baum et al., 2008; Bezak et al., 2016;  
10    Bogaard et al., 2018; Cuomo et al., 2021; Liang et al., 2021; Medina et al., 2021; Pinho et al.,  
11    2022; Tufano et al., 2021; Wang et al., 2013; Zhang et al., 2021; Zhang et al., 2019; Moeineddin et  
12    al., 2023; Li et al., 2025). However, there are still several unresolved issues in regional landslide  
13    forecasting, making accurate and efficient warnings a significant global challenge.

14        The first major issue is the selection of forecasting methods. The presented statistical  
15    approaches generally depend on historical precipitation and landslide inventory data to construct  
16    the rainfall threshold curves. Recently, researchers proposed different types of rainfall threshold  
17    curves, including Intensity-Duration(I-D), Rainfall event-Duration (E-D), Rainfall event-Intensity,  
18    (E-I), Intraday rainfall and antecedent effective rainfall (IR-AER), Intensity-Probability (I-P), and  
19    Intensity-Duration-Mean areal rainfall( I-D-MEAR)(Brunetti et al., 2010; Hong et al., 2005; Rosi  
20    et al., 2020; Zhuang et al., 2014). The I-D curve is the most extensively used among these types.  
21    The I-D curve is typically fitted in either Cartesian coordinates or a double-logarithmic coordinate  
22    system, and the equation of the curve is governed by two key fitting parameters,  $\alpha$  and  $\beta$ ,  
23    expressed as follows:

$$24 \qquad I = \alpha D^\beta \qquad (1)$$

25        where  $\alpha$  and  $\beta$  are derived from the statistical analysis of historical rainfall and landslide data.

26        Studies indicate that statistical methods are applicable in regions with abundant historical  
27    records of rainfall landslides because these areas can provide sufficient samples for fitting the I-D  
28    curve(Bezak et al., 2016; Hong et al., 2017; Kanungo et al., 2014; Kim et al., 2020; Ma et al.,  
29    2015; Marra, 2018; Pradhan et al., 2018). However, in the poor mountainous regions of the Third  
30    World, many areas that are severely affected by landslides lack professional monitoring devices

1 and rain gauges, potentially limiting the application of statistical approaches(Zhang et al., 2021;  
2 Zhang et al., 2019). In contrast, physical methods typically rely on hydrological and mechanical  
3 analyses to calculate the safety factors of landslides under different rainfall scenarios, thereby  
4 reducing the reliance on historical rainfall and landslide observation data. In regions where  
5 landslide inventory data are scarce, physical methods could serve as promising alternatives (Zhang  
6 et al., 2021; Zhang et al., 2019). However, physical methods require historical landslide data to  
7 validate the accuracy of the forecasting results, and the safety factor calculation process typically  
8 requires a considerable amount of time. This computational burden increases substantially when  
9 considering the stability analysis of thousands of slopes at the regional scale, making it difficult to  
10 ensure the efficiency of real-time warnings (Zhang et al., 2021).

11 The second issue pertains to the selection of prediction unit. Clearly defined prediction units  
12 enable residents to identify the specific locations where landslides are likely to occur while also  
13 providing guidance for local governments to develop emergency schemes. However, the I-D  
14 warning curves derived from statistical methods can only provide general trends of hazards within  
15 the region but cannot pinpoint the specific locations of landslide occurrences. Grid cells improve  
16 the clarity of the prediction results to some extent, as the specific locations of each grid within the  
17 area are well defined (Zhang et al., 2021). Researchers have employed grid cells to establish  
18 multiple physical forecasting models such as Shallow Landslide Stability model (Montgomery et  
19 al., 1994), Stability Index Mapping (SINMAP) (Tarboton et al., 1970), The Three-dimensional  
20 Fully Distributed Hydrological model-Safety factor(GEOTop-FS)(Rigon et al., 2006), Transient  
21 Rainfall Infiltration and Grid-Based Regional Slope-Stability Analysis(TRIGRS)(Baum et al.,  
22 2008), High Resolution Slope Stability Simulator(HIRESSS) (Rossi et al., 2013), Hillslope-scale  
23 Shallow Landslide Induced Debris Flow Risk Evaluation(H-slider)(Liang et al., 2021), Open and  
24 Distributed Hydrological Simulation and Landslides (SHIA\_Landslide) (Aristizábal et al., 2016),  
25 Shallow Landslides Instability Prediction (SLIP)(Montrasio et al., 2016), and Fast Shallow  
26 Landslide Assessment Model (FSLAM)(Guo et al., 2022). However, the morphology of grid cells  
27 does not accurately characterize the topographical features of natural hillslopes (Domènech et al.,  
28 2019; Zhang et al., 2021), resulting in a lack of clear geomorphological significance. In practical  
29 applications, a natural slope can be segmented into a series of grid cells, in which each grid is  
30 assigned a different alert level. This indicates that a high warning level in a grid cell does not

1 mean that the entire slope will experience a slide.

2 In contrast, slope units can represent the topographical features of landslides more accurately,  
3 and their boundaries are easily discernible in field environments. Currently, there are various  
4 methods for extracting slope units, including the DEM-based hydrological process analysis  
5 method(Turel et al., 2011), r.slopeunits method(Alvioli et al., 2020), curvature watershed  
6 methods(Yan et al., 2021), MIA-HSU methods(Wang et al., 2019), and multi-scale image  
7 segmentation methods (Huang et al., 2021). In recent years, researchers have developed  
8 forecasting models utilizing slope units, validating their promising application potential in  
9 predicting rainfall-induced landslides (Wang et al., 2023; Zhang et al., 2021).

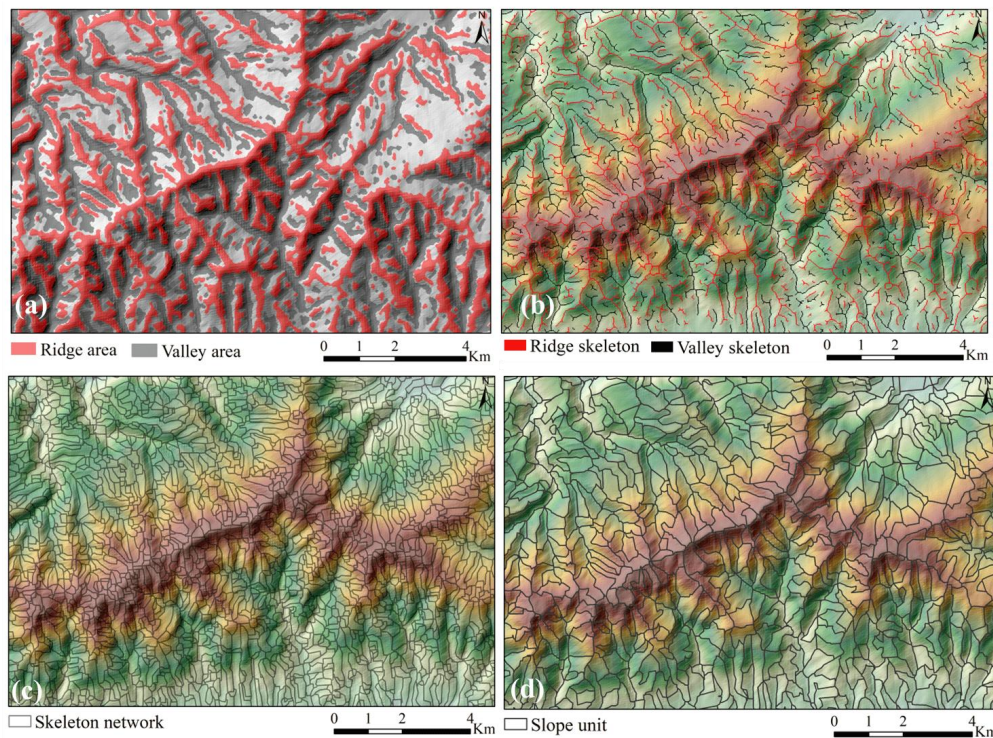
10 Addressing the issues outlined in regional landslide forecasting, this study focuses on the  
11 integration of slope units, physical methods, and rainfall parameterized warning techniques to  
12 develop a rapid forecasting model applicable to large areas on a scale of thousands of square  
13 kilometers. Within this model, we no longer pay attention to the positional relationship between  
14 the rainfall data of a landslide and the I-D curve, but concentrate on the key fitting parameters  $\alpha$   
15 and  $\beta$  of the I-D curve for each slope unit. To facilitate this, we developed a rainfall infiltration  
16 simulation technique rooted in grid cells within slope units and subsequently utilized physical  
17 methods to analyze the instability probability for slope units under different rainfall scenarios. For  
18 each slope unit, we designed rainfall scenarios comprising various antecedent rainfall levels  
19 combined with hundreds of rainfall intensity and duration combinations. This allowed us to obtain  
20 the key parameters  $\alpha$  and  $\beta$  of the I-D curves for different rainfall scenarios, thereby constructing a  
21 database of parameters  $\alpha$  and  $\beta$  under various antecedent precipitation levels. A case study in  
22 Fengjie County, in the Three Gorges Reservoir area, was conducted to validate the reliability of  
23 the proposed method. This research is expected to provide valuable insights for regional landslide  
24 forecasting in impoverished mountainous areas in the developing world.

## 25 **2 Methodology**

### 26 **2.1 The slope unit extraction method MIA-HSU**

27 In this study, we employed the MIA-HSU method to extract slope units(Wang et al., 2021;  
28 Wang et al., 2019; Wang et al., 2023). In the MIA-HSU method, each HSU(homogeneous slope  
29 unit) is defined as a continuous and homogeneous geomorphological entity. This definition implies  
30 that terrain features related to slope and aspect are uniform within each HSU, with boundaries

1 indicating transitions in topographical features. The MIA-HSU method consists of two steps. The  
 2 first step involves partitioning the Digital Elevation Model (DEM) into small regions with  
 3 homogeneous terrain characteristics. In this step, the MIA-HSU method utilizes terrain curvature  
 4 analysis to identify ridge and valley regions (Figure 1a) and then extracts the morphological  
 5 skeleton lines of ridge and valley areas to characterize topographic relief. Morphological  
 6 algorithms (such as dilation and erosion) were used to extract the morphological skeletons of  
 7 ridges, valleys, and flat areas from the DEM (Figure 1b), ultimately connecting these skeletons  
 8 into a closed network (Figure 1c). Thus, each small region within the network exhibits uniform  
 9 geomorphological characteristics. The second step involves merging small adjacent regions. The  
 10 MIA-HSU method employs the principal component analysis (PCA) method to derive fitted  
 11 planes from localized terrain regions, followed by the implementation of vector similarity criteria  
 12 to merge adjacent small regions, thereby generating HSUs(Figure 1d).



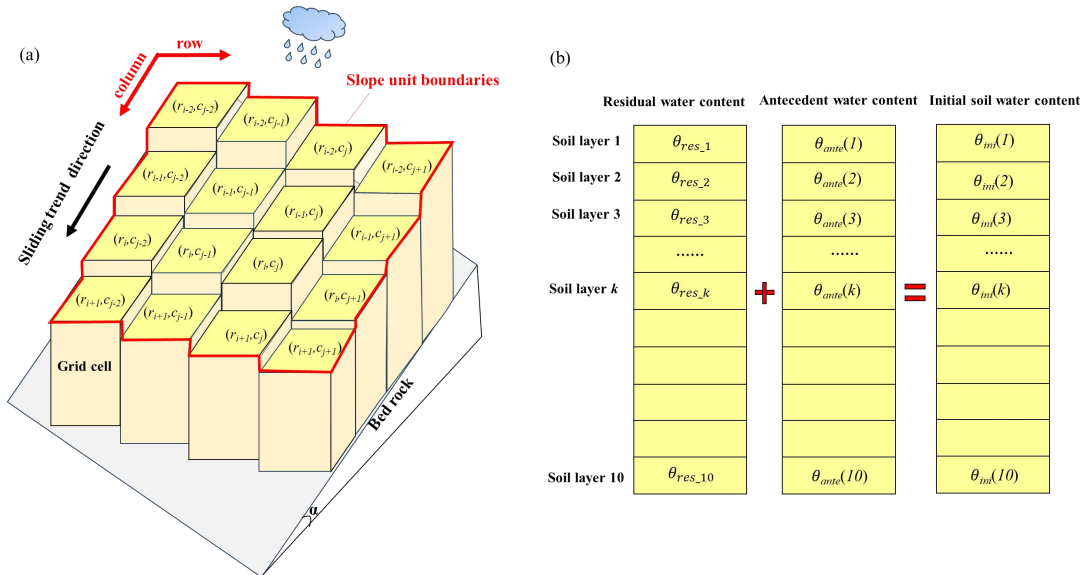
13 Figure 1 HSU extraction process: a. the identification of ridge and valley areas; b. the morphological skeleton line  
 14 extraction for ridge and valley areas; c. the morphological skeleton closed network; d. HSU extraction result  
 15

## 16 2.2 The HSU hydrologic simulation technique based on grid cells

### 17 (1) The identification for row and column information of grid cell within HSUs

18 From a geometric perspective, an HSU can be regarded as a spatial polygon that signifies a  
 19 landform entity with homogeneous terrain features in the field environment. At the regional scale,  
 20 there is obvious heterogeneity in the topography and boundary characteristics among different

1 HSUs(Wang et al., 2021; Wang et al., 2019; Wang et al., 2023), resulting in the immaturity of  
 2 hydrological analysis methods based on slope units. In contrast, hydrological analysis methods  
 3 based on grid cells are well-developed. Some researchers have employed grid cells integrated with  
 4 an infinite slope model or the limit equilibrium method to conduct regional landslide assessment  
 5 or prediction(Gu et al., 2014; Wang et al., 2023; Zhang et al., 2021; Zhuang et al., 2016). In this  
 6 study, each HSU was conceptualized as a composition of grid cells with similar microtopographic  
 7 features, as illustrated in Figure 2a. For each HSU, we utilized GIS spatial analysis tools to  
 8 quantify the number of grid cells contained within it and their corresponding row and column  
 9 positional information, thus establishing a comprehensive database that includes the position  
 10 information of the grid cells within each HSU.



11  
 12 Figure 2 The diagram for HSU-grid cell hydrological connection: a. Grid cells contained within HSU ( $r_i$ ,  $c_j$   
 13 represent the row and column of grid cells contained within HSU, respectively)

14 **(2) Initial water content assignment of HSUs**

15 After obtaining the grid cell information contained within each HSU, conducting a rainfall  
 16 infiltration analysis for these grid cells represents a complex and important task. One issue that  
 17 cannot be overlooked is initial moisture content. For landslides in the Three Gorges Reservoir area  
 18 of China, the soil typically experiences a prolonged dry winter before the rainy season (May to  
 19 September). Previous research indicates that the residual moisture content of slopes before the  
 20 rainy season averages approximately 7% to 8% (Wang et al., 2023). Accordingly, this study  
 21 categorizes the initial water content into two components: the residual moisture content ( $\theta_{res}$ ) and  
 22 the moisture content increment caused by antecedent precipitation( $\theta_{ante}$ ). Here,  $\theta_{res}$  reflects the

1 average moisture level of the soil prior to the rainy season, while  $\theta_{\text{ante}}$  indicate the increase in  
 2 moisture content due to antecedent effective precipitation prior to landslide occurrence.

3 In this study, each grid cell is stratified into ten soil layers, each with a thickness of 0.2 m  
 4 (Figure 2b). For the Three Gorges Reservoir area, the regional landslides triggered by rainfall  
 5 were mainly shallow (with thicknesses of 2-3 m). Therefore, variations in residual moisture  
 6 content within the soil depth were disregarded, and the same residual moisture content value was  
 7 assigned to each soil layer. Following this, we applied steady-state infiltration theory to simulate  
 8 the distribution of moisture content across the soil layers influenced by antecedent precipitation,  
 9 thereby allocating the antecedent rainfall to each soil layer. The calculation for  $\theta_{\text{ini}}$  of each soil  
 10 layer within the grid cell is as follows:

$$11 \quad \theta_{\text{ini}}(k) = \theta_{\text{ante}}(k) + \theta_{\text{res}} \quad (k=1,2,3\dots n) \quad (2)$$

12 Where  $n$  represents the number of soil layers, and here  $n = 10$ ;  $\theta_{\text{ini}}(k)$  indicates the initial  
 13 moisture content of each soil layer;  $\theta_{\text{ante}}(k)$  refers to the moisture change in each soil layer due to  
 14 previous precipitation;  $\theta_{\text{res}}$  stands for the residual moisture content in the grid cell.

### 15 (3) Rainfall infiltration process simulation of grid cell

16 After obtaining the initial moisture content distribution, the 1-dimensional Richards  
 17 infiltration equation was used to solve the moisture content distribution in the grid cell during the  
 18 rainfall infiltration process.

$$19 \quad \frac{\partial \theta}{\partial t} = \frac{\partial}{\partial z} \left[ D(\theta) \cdot \frac{\partial \theta}{\partial z} \right] - \frac{\partial K(\theta)}{\partial z} \quad (3)$$

20 Where  $D(\theta)$  represents the value of soil water diffusivity under unsaturated conditions and  
 21 has  $D(\theta) = K(\theta) / \frac{d\theta}{d\psi_m}$ .

22 The finite difference scheme outlined above was formulated for numerical simulation of  
 23 hydrological processes. The lower boundary, identified as impermeable, is based on the maximum  
 24 soil depth of the grid cell. The upper boundary of each grid cell was designated as an infiltration  
 25 boundary. When the rainfall intensity  $I(t)$  is less than the infiltration capacity of the topsoil, all  
 26 precipitation infiltrates into the soil, and no runoff is generated. In this scenario, the infiltration  
 27 boundary of precipitation was governed by the following differential equation:

$$28 \quad -D(\theta) \frac{\partial \theta}{\partial z} + K(\theta) = I(t) \quad (4)$$

29 When the rainfall intensity exceeded the soil infiltration capacity, the excess portion was

1 transformed into overland flow. At this point, the rainfall infiltration boundary was governed by  
2 the following equation:

$$3 \quad \theta = \theta_s \quad (5)$$

4 Where  $\theta_s$  is the saturated water content of the grid cell.

#### 5 (4) Soil water content generation of HSU

6 Following the calculation of the soil moisture for individual grid cells, the soil water  
7 distribution of the HSU was computed as follows:

$$8 \quad \theta_{HSU}(k) = \frac{\sum_{k=1}^n \theta(k)}{n} \quad (6)$$

9 where  $\theta_{HSU}(k)$  represents the moisture content of the  $k$ th layer of the HSU,  $\theta(k)$  denotes the  
10 moisture content of the  $k$ th layer in the grid cell.  $n$  is the number of soil layers ( $n = 10$ ).

### 11 2.3 *HSU<sub>prob</sub>*: the calculation of instability probability of HSUs

#### 12 (1) Profile extraction

13 After calculating the soil water content within each HSU, analyzing the stability of HSUs  
14 during the rainfall infiltration process is another important task. At present, the time required to  
15 carry out 3D analysis for each HSU on a large regional scale is too large, so extracting the  
16 calculation profile of the HSU becomes a reasonable selection. Currently, there is no uniform  
17 method for extracting the calculation profile of HSUs. Some reasonable assumptions are  
18 summarized as follows: the position of the profile line should reflect the elevation difference  
19 between the front and back edges of the slope, and the centroid point of the HSUs should be on the  
20 calculated profile to ensure that the soil weight on both sides of the calculated section is relatively  
21 uniform, and the areas of the two sections should be close to each other.

22 Based on these considerations, we developed a fast extraction algorithm HSU-profile (Wang  
23 et al., 2021; Wang et al., 2023) for HSU profiles at large regional scales, which can be divided into  
24 three steps:

25 First, the highest elevation point  $H$  of the HSU polygon is connected to centroid point  $C$  to  
26 obtain line segment  $L_1$ , which intersects the HSU polygon at point  $J_1$  (Figure 3b). Line segment  $L_1$   
27 divides the HSU polygon into two parts, and the areas of the two parts,  $S_1$  and  $S_2$  are calculated  
28 to obtain the area ratio  $A = S_1 / S_2$ .

29 Next, the lowest elevation point  $L$  and centroid  $C$  are connected to form line segment  $L_2$ , as

1 shown in Figure 3 b. Determine the intersection point  $J_2$  between  $L_2$  and the polygon of the slope  
 2 unit is determined. At this point, the HSU was divided into two parts by line segment  $L_2$ , and the  
 3 areas of the two parts,  $S_3$  and  $S_4$ , were calculated to obtain the area ratio  $B=S_3/S_4$ .

4 Finally,  $|A|$  and  $|B|$  are compared. A smaller absolute value of A indicates that line segment  $L_1$   
 5 divides the areas on both sides of the HSU polygon more evenly. In this case,  $L_1$  is selected as the  
 6 profile line. Otherwise, the line segment  $L_2$  was chosen as the profile line.

7 (2) Calculation of safety factor  $F_s$  calculation

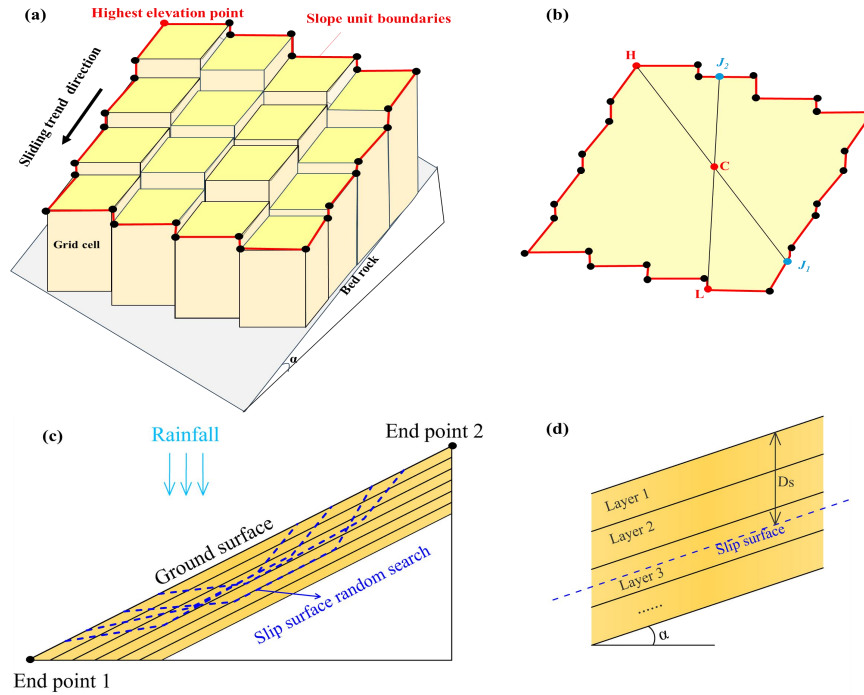
8 For each HSU, the Monte Carlo method was used to generate a large number of potential  
 9 polyline-type slip surfaces (Figure 3c), and the random walk method(Greco, 1996; Zhang et  
 10 al.,2006) was employed to search for the critical slip surface. The infinite slope model was used to  
 11 calculate the safety factor  $F_s$  of each potential slip surface as follows:

$$12 \quad F_s = \frac{\tan \varphi}{\tan \alpha} + \frac{c + u_s \tan(\varphi^b)}{\gamma_s D_s \cos \alpha \sin \alpha} \quad (7)$$

13 where  $c$  is the effective cohesion of the soil,  $\varphi$  is the effective internal friction angle of the  
 14 soil, and  $r_s$  is the average unit weight of soil above the slip surface.  $\varphi^b$  is related to the matric  
 15 suction; when the matric suction is low, it is close to the internal friction angle(Zhang et al., 2018).  
 16  $D_s$  is the thickness of the soil layer above the slip surface.  $u_s$  represent the matric suction, which  
 17 can be described by the Van Genuchten model(Van Genuchten, 1980):

$$18 \quad S_e = \frac{\theta - \theta_r}{\theta_s - \theta_r} = \left[ \frac{1}{1 + (\alpha_w \times u_s)^n} \right]^m \quad (8)$$

19 Where  $S_e$  represents the saturation degree,  $\theta$  denotes the soil water content of the HSU,  
 20  $\theta_s$  and  $\theta_r$  are the saturated and residual water content, respectively. The parameters  $\alpha_w$ ,  $n$  and  $m$   
 21 characterize the shape of the soil–water characteristic curve, with the relationship  $n=1-1/m$  .



1  
2 Figure 3 HSU instability probability calculation diagram a. Extraction of HSU boundary points; b. Profile line  
3 extraction of HSU polygon; c. Random search for critical slip surface; d. Enlarged view of the sliding mass for  
4 detailed visualization.

5 (3)  $HSU_{prob}$  calculation

6 According to the saturated-unsaturated rainfall infiltration theory, the mechanical parameters  
7 of the soil (such as cohesion force  $c(kPa)$  and internal friction angle  $\varphi(^{\circ})$ ) are significantly affected  
8 by soil moisture content fluctuations. The variation in soil mechanical parameters during the  
9 process of rainfall infiltration is very complex, and it is generally acknowledged that dry soil prior  
10 to rainfall infiltration exhibits higher mechanical strength (characterized by elevated parameter  
11 values). As rainwater continues to infiltrate, the soil water content gradually increases, leading to a  
12 decreasing trend in mechanical parameters, such as cohesion and internal friction angle.  
13 Consequently, the mechanical parameters of the soil within each HSU are not fixed, but spatial  
14 uncertainty exists to some extent. In this context, employing probabilistic analysis methods to  
15 calculate the instability probability of an HSU is a more reasonable choice. Probability density  
16 functions (such as normal or uniform distributions) are commonly used to describe the uncertainty  
17 of the geotechnical parameters. The normal distribution is considered suitable for small areas or  
18 watersheds where hydrogeological parameters can be collected in detail, whereas a uniform  
19 distribution is more applicable for larger areas, where it is difficult to acquire detailed  
20 hydromechanical parameters(Wang et al., 2021; Wang et al., 2023).

1 In this study, we utilized a uniform distribution to simulate the uncertainty of the mechanical  
 2 parameters within the HSUs. The soil mechanical parameters in the unsaturated state before  
 3 rainfall were taken as the upper bound, while those in the fully saturated state were considered the  
 4 lower bound, thereby establishing the upper and lower value boundaries for the mechanical  
 5 parameters within the HSU, as indicated in Equations (9) and (10):

$$6 \quad c \in [c_{lower}, c_{upper}] \quad (9)$$

$$7 \quad \varphi \in [\varphi_{lower}, \varphi_{upper}] \quad (10)$$

8 where  $c_{upper}$  and  $c_{lower}$  represent the upper and lower bounds of  $c$ (kPa), respectively,  $\varphi_{upper}$  and  
 9  $\varphi_{lower}$  represent the upper and lower bounds of  $\varphi$ (°), respectively. The Monte Carlo method was  
 10 employed to randomly select the values within these bounds. The instability probability of the  
 11 HSU was calculated using Equation (11).

$$12 \quad HSU_{prob} = \frac{Sum_{Fs < 1}}{m} \quad (11)$$

13 where  $m$  represents the number of random selections for the mechanical parameters and  $m$   
 14 is set to 500.

#### 15 **2.4 The obtainment of key fitting parameters $\alpha$ and $\beta$ for I-D curves of HSUs**

16 In this study, an HSU is regarded as unstable when the value of  $HSU_{prob}$  exceeds 50%. Then,  
 17 the rainfall intensity and duration data with HSU instability under different rainfall scenarios were  
 18 recorded to obtain the key fitting parameters  $\alpha$  and  $\beta$  for the I-D curves of each HSU, thereby  
 19 establishing a database of parameters  $\alpha$  and  $\beta$ . The detailed steps are as follows.

##### 20 (1) Setting the antecedent effective rainfall levels $AER\_i(i=1,2,3\dots n)$

21 The antecedent effective rainfall(AER) has a significant impact on landslide occurrence.  
 22 Previous research indicates that in the Three Gorges Reservoir area, the minimum value of AER  
 23 before landslide occurrence is 0 mm, whereas the maximum value of AER can exceed 170  
 24 mm(Wang et al., 2021). Therefore, 20 different levels of AER ranging from 0 to 200 mm were  
 25 established with intervals of 10 mm.

##### 26 (2) Design of the combination of rainfall intensity (I) and duration(D)

27 For each antecedent rainfall level, we categorized rainfall intensity (I) into eight levels to  
 28 represent the variation from light to heavy rainstorms: 2, 5, 10, 20, 30, 40, 50, and 60 mm/h. The  
 29 rainfall duration (D) ranged from 1 to 24 h, with intervals of one hour. Consequently, 192

1 combinations of I and D were generated for each AER level.

2 (3) Generation of fitting parameters  $\alpha$ ,  $\beta$  of the I-D curves

3 For each combination of rainfall intensity and duration data, the method outlined in Section  
4 2.2 is used to determine the soil water distribution within each HSU, and the corresponding value  
5 of  $HSU_{prob}$  was computed using the method described in Section 2.3. If the HSU is unstable, the  
6 corresponding intensity and duration data can serve as data points for fitting the I-D curves.  
7 Subsequently, a power function was utilized to fit these data points to obtain the key fitting  
8 parameters  $\alpha$  and  $\beta$  of the I-D curve. As presented above, the fitting parameters  $\alpha$  and  $\beta$  for the I-D  
9 curve of each HSU can be generated, thereby establishing a database for  $\alpha$  and  $\beta$  at different AER  
10 levels.

### 11 **2.5 Warning Mode**

12 In practical applications, the antecedent effective rainfall(AER), rainfall intensity (I), and  
13 duration (D) for each HSU can be computed using Quantitative Precipitation Estimation (QPE)  
14 and Quantitative Precipitation Forecasting (QPF) products provided by the meteorological  
15 department (Wang et al., 2021). Next, we analyzed the relationship between the actual value of  
16 AER and the 20 levels of AER documented in the database, thereby determining the level that is  
17 closest to the antecedent effective rainfall data of the HSU. The  $\alpha$  and  $\beta$  values corresponding to  
18 this level were retrieved from the database for the following assessments.

19 (1) If  $I \geq \alpha D^\beta$ , the data point (I, D) is above the warning curve; thus, the warning should be  
20 released.

21 (2) Conversely, if  $I < \alpha D^\beta$ , it signifies that the data point (I, D) is below the warning curve;  
22 therefore, no warning should be issued.

23 The programming languages Fortran 95 and Python 3.1 were employed to compile the  
24 algorithms outlined in Sections 2.1-2.5, and the overall flowchart of the warning mode is depicted  
25 in Figure 4.

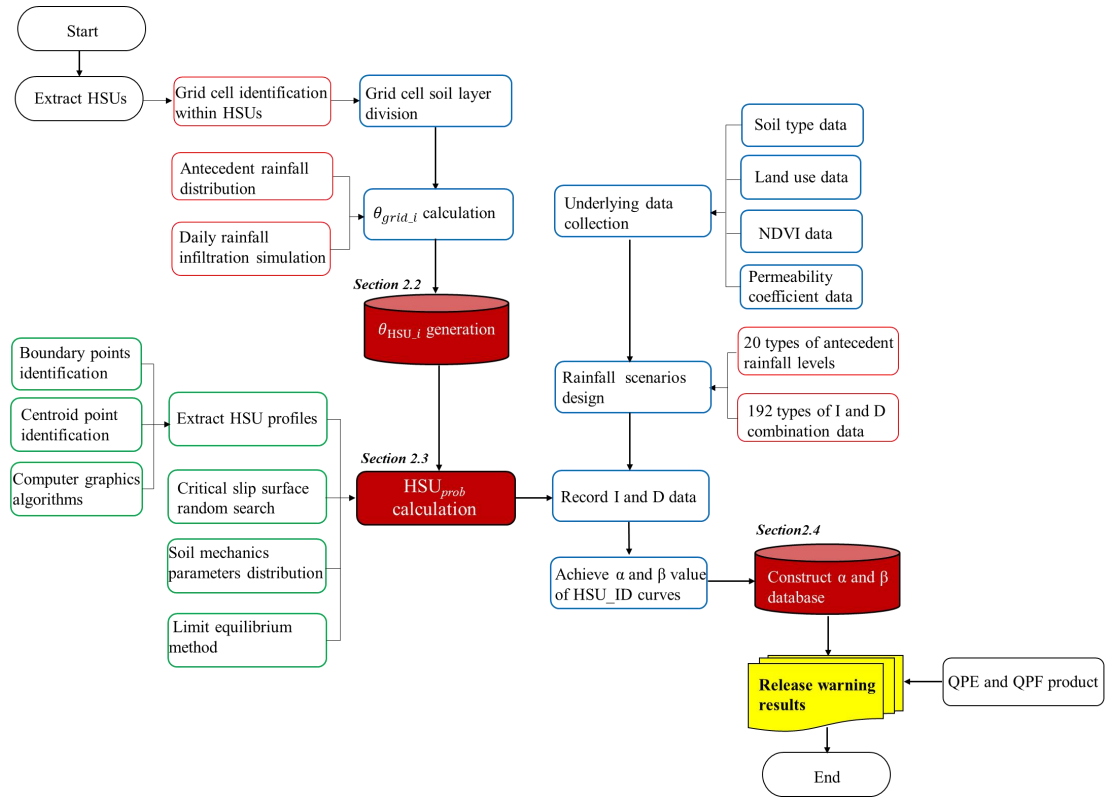


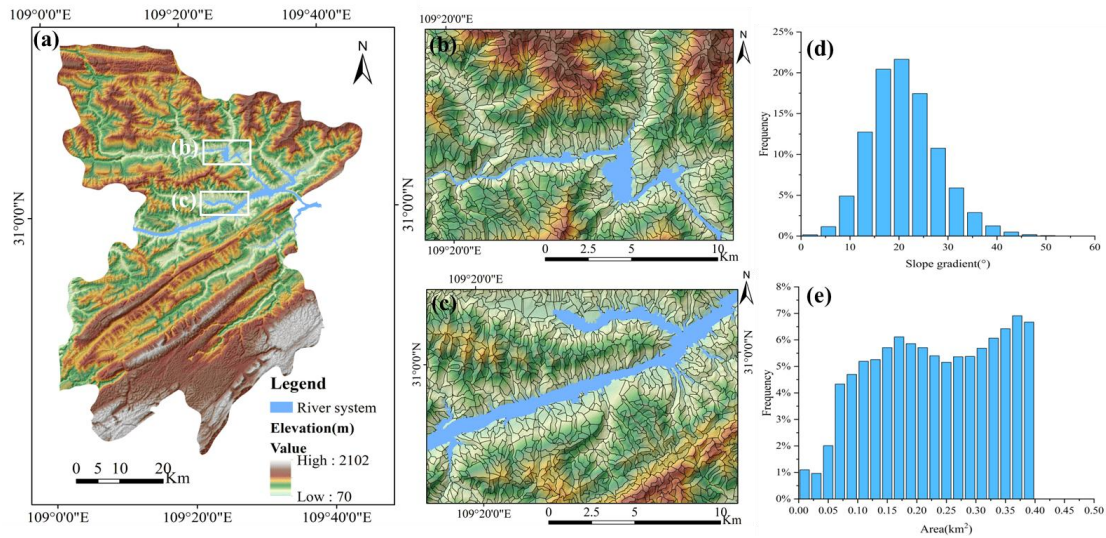
Figure 4 The flow chart of the fast warning mode based on parameter  $\alpha$  and  $\beta$  database

### 3 Study area and data

#### 3.1 Study area and slope unit data

Fengjie County is situated in the eastern region of the Three Gorges Reservoir area, with geographical coordinates ranging from  $109^{\circ}1'17''$  " to  $109^{\circ}45'58''$  East and  $30^{\circ}29'19''$  to  $31^{\circ}22'33''$  North, covering a total area of 4087 km<sup>2</sup>. The region has a subtropical humid monsoon climate with an annual average rainfall of 1,500–2,000 mm. The rainy season occurs from May to September, accounting for 70% of the annual precipitation. The terrain is primarily mountainous and the Yangtze River flows across the region from west to east. Geological hazards, such as landslides, debris flows, and collapses, are widely distributed in Fengjie County, with rainfall landslides posing the most significant threat. Based on the 7m DEM of Fengjie (Figure 5a), the MIA-HSU method was employed to extract the slope units, resulting in the identification of 17,547 HSUs (Figures 5 b and c). Histograms of the slope gradient and area distribution of the HSUs are presented in Figure 5d-e. As shown in Figure 5d, the slope gradients of the HSUs follow a normal distribution, with 85.4% of the slopes falling within the range of  $10^{\circ}$  to  $30^{\circ}$ . Figure 5e illustrates that the average area of the HSUs is 0.23 km<sup>2</sup>, with 53.9% of the slope units having an area less than 0.25 km<sup>2</sup>. Because the sliding depth of shallow landslides typically ranges from 2 m

1 to 3 m, the majority of HSUs can be classified as small-to medium-scale landslides (with volumes  
2 under 500,000 m<sup>3</sup>).

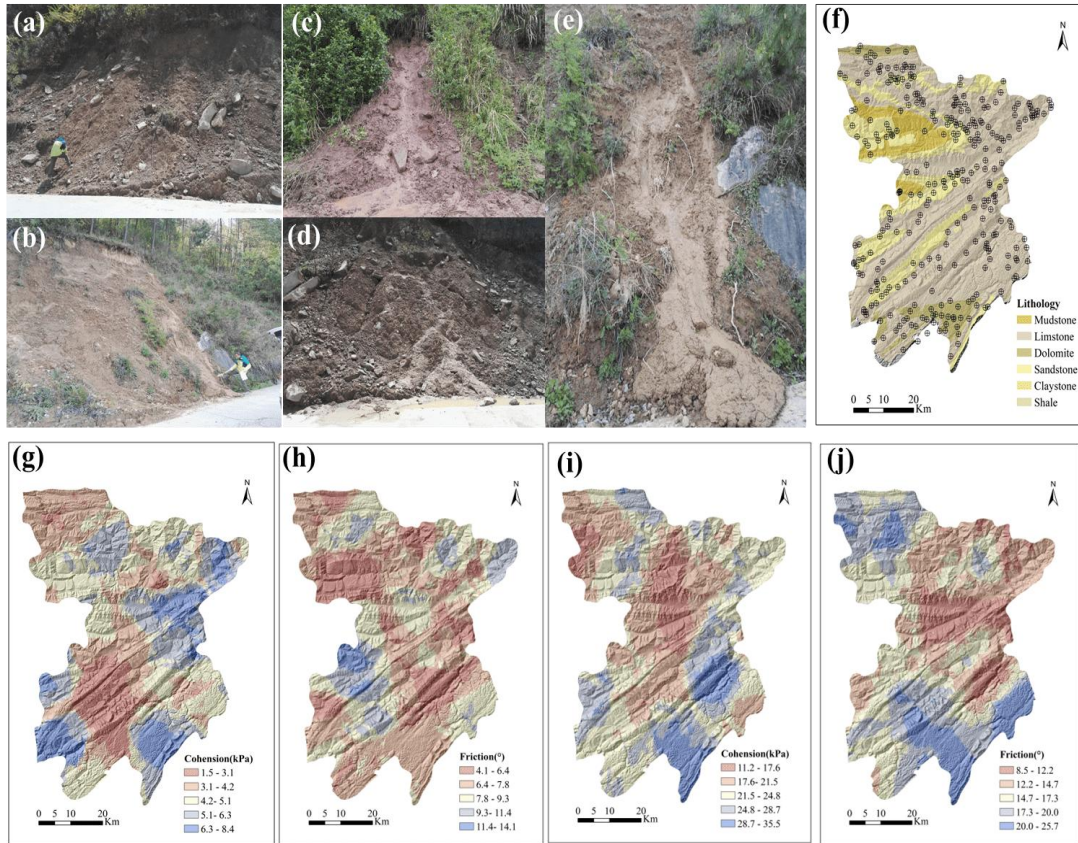


3  
4 Figure 5 Division of HSUs in Fengjie County a. Fengjie DEM; b and c. Extraction results for selected regions:  
5 Enlarged View; d. Histogram of slope distribution of HSUs; e. Histogram of area distribution of HSUs.

### 6 3.2 Soil mechanical parameter $c$ (kPa) and $\phi$ (°) data of HSUs

7 The rainfall-triggered shallow landslides within the study area are mainly composed of  
8 quaternary clay and silt, which are classified as fine-grained soils(Wang et al., 2021; Wang et al.,  
9 2023). Field investigations indicate that the sliding soil is fully or even oversaturated, with some  
10 soil mass transitioning into mudflow during the sliding process. The laboratory moisture content  
11 tests revealed that the soil water content under these conditions approached or exceeded the liquid  
12 limit. To obtain detailed soil mechanical parameters under different moisture states, we conducted  
13 extensive field sampling across Fengjie County, resulting in 312 sampling points, as depicted in  
14 Figure 6f. For each sampling point, direct laboratory shear tests were performed to derive the soil  
15 mechanical parameters  $c$  (kPa) and  $\phi$  (°) at the liquid and plastic limits, respectively. Based on  
16 geological survey data provided by the Fengjie County Land Bureau, the dry density of soil within  
17 a 10-meter thickness ranges from 1.7 to 1.8 g/cm<sup>3</sup>(Wang et al.,2021). Therefore, the dry density of  
18 each soil samples is randomly selected within this range. In accordance with the ASTM-d6528  
19 (ASTM, 2017) standard, 312 groups of liquid-plastic limit tests and 624 groups of undrained  
20 direct shear tests were performed to obtain the mechanical parameters of each sample at both the  
21 liquid and plastic limit water contents. Subsequently, ArcGIS spatial analysis tools were utilized to  
22 generate distribution maps of  $c$  (kPa) and  $\phi$  (°) under plastic and liquid limit moisture conditions,

1 as shown in Figures 6g-j.



2  
3 Figure 6 State of Landslide Soil Before and After Rainfall (a. Soil approaching plastic limit moisture content  
4 before rainfall; b. Soil approaching plastic limit moisture content before rainfall; c. Soil in a fluid state after  
5 rainfall; d. Soil in a fluid state after rainfall; e. Fully saturated and liquefied soil after rainfall; f. Soil sampling  
6 locations; g.  $c$  (kPa) at plastic limit moisture content; h.  $\phi$  ( $^{\circ}$ ) at plastic limit moisture content; i.  $c$  (kPa) at liquid  
7 limit moisture content; j.  $\phi$  ( $^{\circ}$ ) at liquid limit moisture content.)

### 8 3.3 Rainfall data

9 Rainfall data sources include Quantitative Precipitation Forecasting (QPF) products and  
10 Quantitative Precipitation Estimation (QPE) products. The QPF product obtained from the local  
11 government of Fengjie County is typically utilized to forecast future rainfall at a regional scale,  
12 which can provide rainfall forecast products for the next hour. QPE data are applied to estimate  
13 historical regional rainfall at a regional scale and are essential for determining the antecedent  
14 effective rainfall (AER), which can be computed as follows:

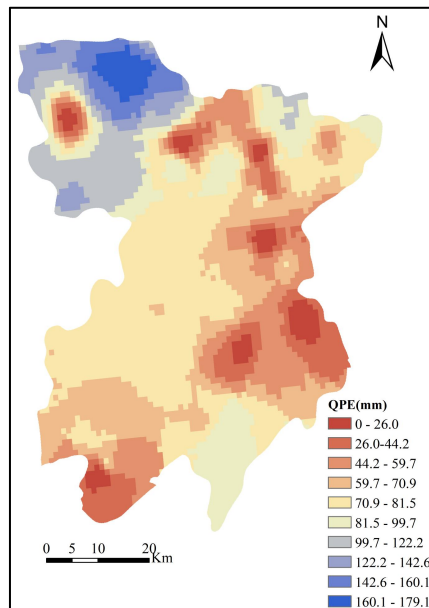
$$15 \quad AER = \sum_{i=1}^n a^n R_i \quad (12)$$

16 Where AER is the antecedent effective rainfall,  $a$  is the attenuation coefficient, which is equal  
17 to 0.84, based on the research of the Fengjie count (Wang et al., 2021),  $n$  is the number of days

1 before the landslide occurs.

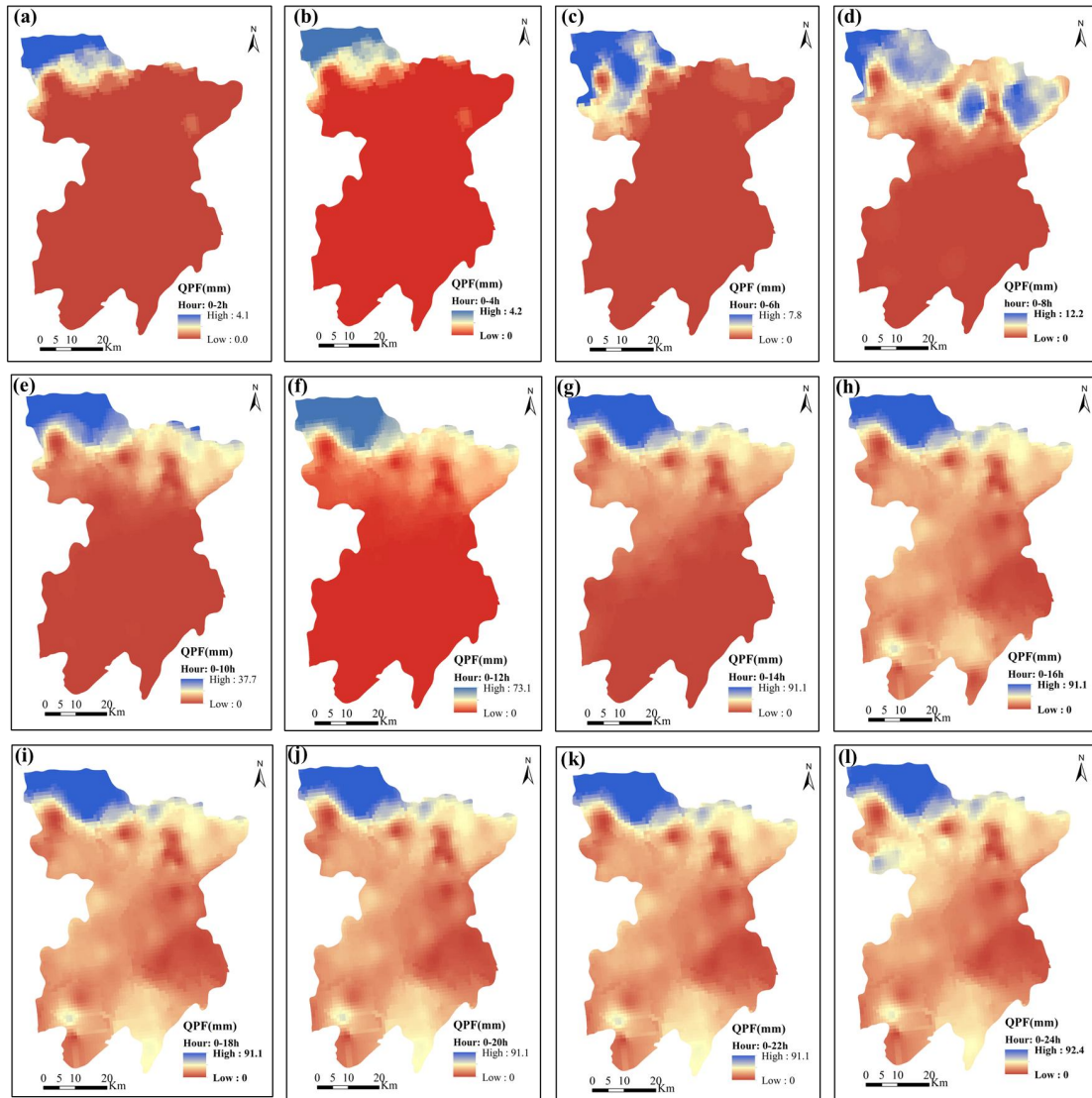
2 **4 Case study: Rainfall-induced landslides of 31 August, 2014**

3 From August 30–31, 2014, Fengjie experienced continuous heavy rainfall, triggering a  
4 series of landslide hazards that resulted in over 30 fatalities and an economic loss of 580 million  
5 yuan. Based on the daily QPE data for August 15-31, the effective precipitation for the 15 days  
6 prior to the landslide hazards is shown in Figure 7. As illustrated in Figure 7, the maximum  
7 precipitation during this period was 179.10 mm, which occurred in the northwestern region of the  
8 area. The hourly QPF data for August 31 are presented in Figure 8 *a-l*. As illustrated in Figure 8  
9 *a-d*, the rainfall was minimal from 00:00 to 08:00, with a maximum cumulative rainfall of 12.2  
10 mm 08:00. As shown in Figures 8e-g, rainfall began to increase rapidly at 10:00, reaching a  
11 maximum cumulative precipitation of 92.40 mm by 14:00 in the northwestern region of Fengjie  
12 County. Figures 8 h-l indicate that from 16:00 to 24:00, the cumulative rainfall remained constant,  
13 suggesting that the rainfall process had ceased.



14

15 Figure 7 Precipitation Data Processing (Effective Precipitation from August 15 to August 30, 2014)

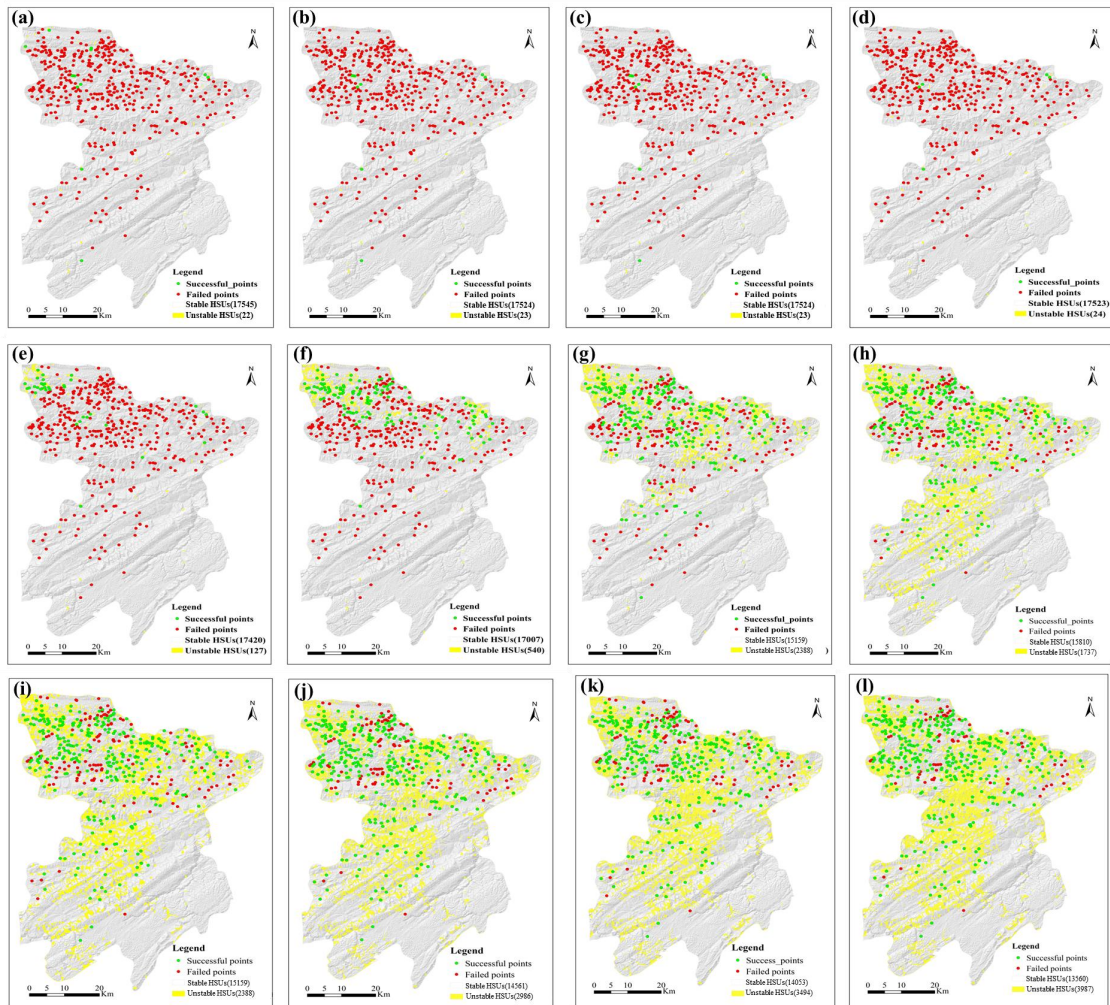


1  
 2 Figure 8 Radar forecast precipitation data for 2014/08/31 (a. 2:00; b. 4:00; c. 6:00; d. 8:00; e. 10:00; f. 12:00; g.  
 3 14:00; h. 16:00; i. 18:00; j. 20:00; k. 22:00; l. 24:00)

4 The Land and Resources Bureau of Fengjie County provided data on landslide points  
 5 triggered by rainfall on August 31. This heavy precipitation triggered 583 landslides, which were  
 6 mainly distributed in the northwestern region (as indicated by the red and green solid points in  
 7 Figure 9). This study utilized the QPE (Figure 7) and QPF data (Figures 8 a-l) as inputs to forecast  
 8 landslide hazards for August 31.

9 The landslide forecast results from 02:00 to 24:00 are shown in Figures 9(a-l). It can be seen  
 10 from Figures 8 and 9 that there is a good correlation between the spatial distribution of unstable  
 11 HSUs and rainfall characteristics. As presented in Figures 9a-d, at the beginning of the rainfall  
 12 process (before 8:00), the majority of the HSUs remained stable owing to the minimal rainfall.  
 13 Unstable HSUs began to emerge in the northwestern region starting at 10:00, coinciding with the

1 rapid increase in rainfall. Additionally, as the rainfall progressed, the number of unstable HSUs  
 2 increased swiftly and spread towards the central and southern regions (Figures 9f-g). Notably,  
 3 many unstable slope units appeared within several hours after heavy rainfall ceased. Figures 9h-l  
 4 reveal that from 16:00 to 24:00, although the heavy rainfall essentially ended, the number of  
 5 unstable HSUs continued to rise because of the moisture infiltration of the saturated top soil,  
 6 reaching a total of 3,987 at 24:00.



7

8 Figure 9 Prediction results at 02:00 to 24:00 (a. 2:00; b. 4:00; c. 6:00; d. 8:00; e. 10:00; f. 12:00; g. 14:00; h. 16:00;  
 9 i. 18:00; j. 20:00; k. 22:00; l. 24:00)

10 This study employs the Receiver Operating Characteristic (ROC) method to analyze the  
 11 predictive performance of the HSU(Fawcett, 2006). For physically model-based slope units, the  
 12 ROC method describes the following four possible states using a contingency table:

13 ① True Positive (TP): HSU contain landslide points and exhibit instability;

14 ② True Negative (TN): HSU does not contain landslide points and does not exhibit instability;

③ False Positive (FP): HSU does not contain landslide points but exhibits instability;

④ False Negative (FN): HSU contains landslide points but does not exhibit instability.

According to GIS spatial statistics, 583 landslides triggered by rainfall on August 31 were contained within 425 HSUs. In this study, these HSUs are taken as benchmark values for the calculation of TP, TN, FP, and FN, and the missing alarm rate (MAR) and false alarm rate (FPR) can be calculated as follows:

$$\text{MAR} = 100\% \times \text{FN} / 425 \quad (13)$$

$$\text{FPR} = 100\% \times \text{FP} / (\text{FP} + \text{TN}) \quad (14)$$

The detailed forecast results for -02-24h are shown in Table 1. As shown in columns 7-8 of Table 1, with increasing rainfall duration, the Missing Alarm Rate (MAR) gradually decreases, while the False Positive Rate (FPR) gradually increases. Taking the result of 24h as an example, the MAR of 24h is 11.8% and the FPR is 21.1%, indicating that the prediction result can satisfy the requirement of early warning practice.

Table 1 Analysis of Forecast Results for the 831 Case Study

| Forecasting hour(h) | Unstable HSUs | TP  | TN    | FP   | FN  | MAR (%) | FPR (%) |
|---------------------|---------------|-----|-------|------|-----|---------|---------|
| 02                  | 22            | 7   | 17097 | 25   | 418 | 98.4    | 0.1     |
| 04                  | 23            | 3   | 17102 | 20   | 422 | 99.3    | 0.1     |
| 06                  | 23            | 3   | 17102 | 20   | 422 | 99.3    | 0.1     |
| 08                  | 24            | 2   | 17100 | 22   | 423 | 99.5    | 0.1     |
| 10                  | 127           | 27  | 17022 | 100  | 398 | 93.6    | 0.6     |
| 12                  | 540           | 116 | 16698 | 424  | 309 | 72.7    | 2.5     |
| 14                  | 1370          | 231 | 15983 | 1139 | 194 | 45.6    | 6.7     |
| 16                  | 1737          | 289 | 15674 | 1448 | 136 | 32.0    | 8.5     |
| 18                  | 2388          | 327 | 15061 | 2061 | 98  | 23.1    | 12.0    |
| 20                  | 2986          | 354 | 14490 | 2632 | 71  | 16.7    | 15.4    |
| 22                  | 3494          | 364 | 13992 | 3130 | 61  | 14.4    | 18.3    |
| 24                  | 3987          | 375 | 13510 | 3612 | 50  | 11.8    | 21.1    |

According to the ROC method, the precision and accuracy of the prediction results were calculated as follows:

$$\text{Precision} = \text{TPR} / (\text{TPR} + \text{FPR}) \quad (15)$$

$$\text{Accuracy} = (\text{TP} + \text{TN}) / (\text{TP} + \text{FN} + \text{TN} + \text{FP}) \quad (16)$$

Table 2 provide the calculation results of precision and accuracy at 24h. As shown, the precision of the forecasting results is 80.7%, with an accuracy value of 79.1%, indicating the proposed warning mode has satisfactory comprehensive forecasting performance.

Table 2 Calculation Results of Precision and Accuracy at the 24th Hour

| Forecasting hour(h) | Unstable HSUs | TP  | TN    | FP   | FN | Precision(%) | Accuracy(%) |
|---------------------|---------------|-----|-------|------|----|--------------|-------------|
| 24                  | 3987          | 375 | 13510 | 3612 | 50 | 80.7         | 79.1        |

## 5 Discussion

### 5.1 The discussion on the computational efficiency

For emergency warnings during the rainy season, the swift release of warning information is crucial for local authorities to develop emergency plans and to evacuate residents from landslide-prone areas. Therefore, local governments not only seek satisfactory accuracy in the warning model but also require minimal time. To evaluate the computational efficiency of the proposed model, a standard laptop was utilized to execute the forecast for landslide hazards on August 31. The device specifications and computation times are presented in Table 3. As shown in Table 3, for the regional scale covering several thousand square kilometers, the prediction model can rapidly complete real-time warnings for the next 24 h within 12 min, indicating that its computational efficiency can satisfy the requirements of emergency warning.

Table 3 Analysis of computational efficiency of the prediction model

| Area (m <sup>2</sup> ) | Number of HSU | CPU              | System                          | Equipment name           | Memory | Run time |
|------------------------|---------------|------------------|---------------------------------|--------------------------|--------|----------|
| 4080                   | 17547         | Intel(R) Core i7 | Windows 64-bit operating system | ThinkPad P15 Workstation | 16G    | <12min   |

### 5.2 Further analysis of prediction performance

Using the 24-hour prediction results as an example, we randomly selected seven HSUs with false alarms for further analysis (Table 4). Columns 3–5 of Table 4 present the effective antecedent rainfall AER of these HSUs, the AER levels assigned by the database, and the relative errors, respectively. As shown in Column 5, the relative error ranges from 0.7% to 6.3%, indicating that the 20 levels of the AER designed in the database can accurately reflect the effective antecedent rainfall characteristics of the HSUs. The average rainfall intensity, duration, and cumulative rainfall data at 24:00 are shown in Columns 6–8. As seen in Column 6, the cumulative rainfall for the seven HSUs ranges from 12 mm to 29.8 mm, with average rainfall intensities range from 0.5 mm/h to 1.25 mm/h, which can be classified as light to moderate rain type. The instability probability ( $HSU_{prob}$ ) of these HSUs was calculated to investigate the causes of false positives. As shown in Column 9, among the seven HSUs with false alarms, five had an instability probability

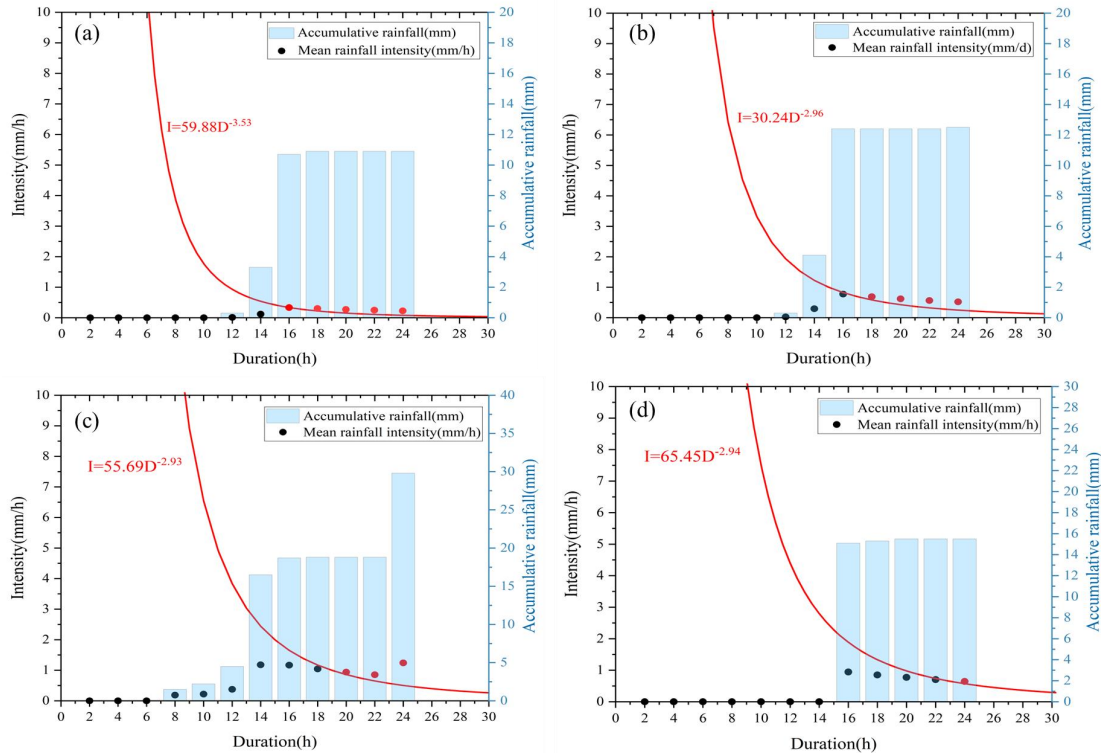
1 of less than 50%, indicating that these HSUs did not experience instability during the rainfall  
 2 process. Therefore, we cautiously conclude that although the prediction model exhibits preferable  
 3 operational efficiency, it may increase the false-positive rate to some extent.

4 Table 4 The selected HSUs that report false alarms at 24:00

| Number of HSUs | Slope gradient (°) | AER assignment  |  |                | Daily accumulated rainfall (mm) | Duration (h) | Rainfall intensity $I$ (mm/h) | HSU <sub>prob</sub> |
|----------------|--------------------|-----------------|--|----------------|---------------------------------|--------------|-------------------------------|---------------------|
|                |                    | Actual AER (mm) | AER levels assigned by the database (mm) | Relative error |                                 |              |                               |                     |
| 6172           | 19.4               | 74.6            | 70                                       | 6.2%           | 24.2                            | 24           | 1.0                           | 0.88                |
| 8561           | 26.5               | 70.9            | 70                                       | 1.3%           | 12.2                            | 24           | 0.5                           | 0.19                |
| 6066           | 26.7               | 83.1            | 80                                       | 3.7%           | 29.8                            | 24           | 1.25                          | 0.65                |
| 8535           | 25.9               | 68.6            | 70                                       | 2.0%           | 10.9                            | 24           | 0.45                          | 0.18                |
| 13108          | 40.3               | 74.1            | 70                                       | 5.5%           | 15.4                            | 24           | 0.64                          | 0.29                |
| 8297           | 23.4               | 70.5            | 70                                       | 0.7%           | 12.0                            | 24           | 0.5                           | 0.14                |
| 12966          | 38.3               | 74.7            | 70                                       | 6.3%           | 14.6                            | 24           | 0.61                          | 0.25                |

5 To investigate the potential for reducing the false-alarm rate, we selected four HSUs from  
 6 Table 4 for further analysis. Figures 10 a-d presented the I-D curves and cumulative precipitation  
 7 distribution histograms for these HSUs.

8 For each HSU, the QPF data from 00:00 to 24:00 were discretized into 12 sets of rainfall  
 9 intensity and duration data points at 2-hour intervals (represented by black and red solid dots). The  
 10 black solid dots positioned below the I-D curve indicate that the HSU is stable at that moment,  
 11 whereas the red solid dots located above the curve signify false alarms at the current forecasting  
 12 hour. As shown in Figures 10a-d, the red false alarm points for the four HSUs are all situated very  
 13 close to the I-D curve, nearly tangent to it. This proximity suggests that slight spatial adjustments  
 14 to these points could alter the forecast results. Another important issue is that some of the black  
 15 solid dots correspond to a cumulative rainfall of 0 mm, indicating that the rainfall process had not  
 16 yet begun. Therefore, it is necessary to adjust the spatial positions of data points I and D based on  
 17 the actual initiation time of the rainfall process, thereby facilitating an in-depth investigation of the  
 18 causes of the false alarms.



1

2 Figure 10 The I-D Curves of HSUs before the adjustment of rainfall process (a. 8535; b. 8561; c. 6066; d.  
3 13108)

4 In this study, an HSU with number 8535 is taken as an example to illustrate the process of  
5 adjusting the spatial positions of data points I and D. As shown in Table 5, the rainfall process for  
6 this HSU started at 12:00 and ended at 24:00 with a duration of 12 h. The start time of rainfall was  
7 used as the starting point to recalculate the rainfall intensity during the rainfall process, as  
8 indicated in the text highlighted with a yellow background in Table 5. The adjusted average  
9 rainfall intensity was significantly higher than the values prior to adjustment. This means that the  
10 adjustment of the rainfall process led to notable changes in the spatial locations of the data points I  
11 and D. As shown in Figure 11a, after updating the positions of data points I and D, the HSU does  
12 not exhibit any false alarms. Figures 11b-d present the updated forecast results for the other three  
13 HSUs after the adjustment. As shown in Figure 11a-d, following the adjustments, three out of  
14 these four HSUs were able to release accurate results. Therefore, we advise that practical warning  
15 applications should consider the influence of the difference in rainfall processes of HSUs on the  
16 prediction results.

17

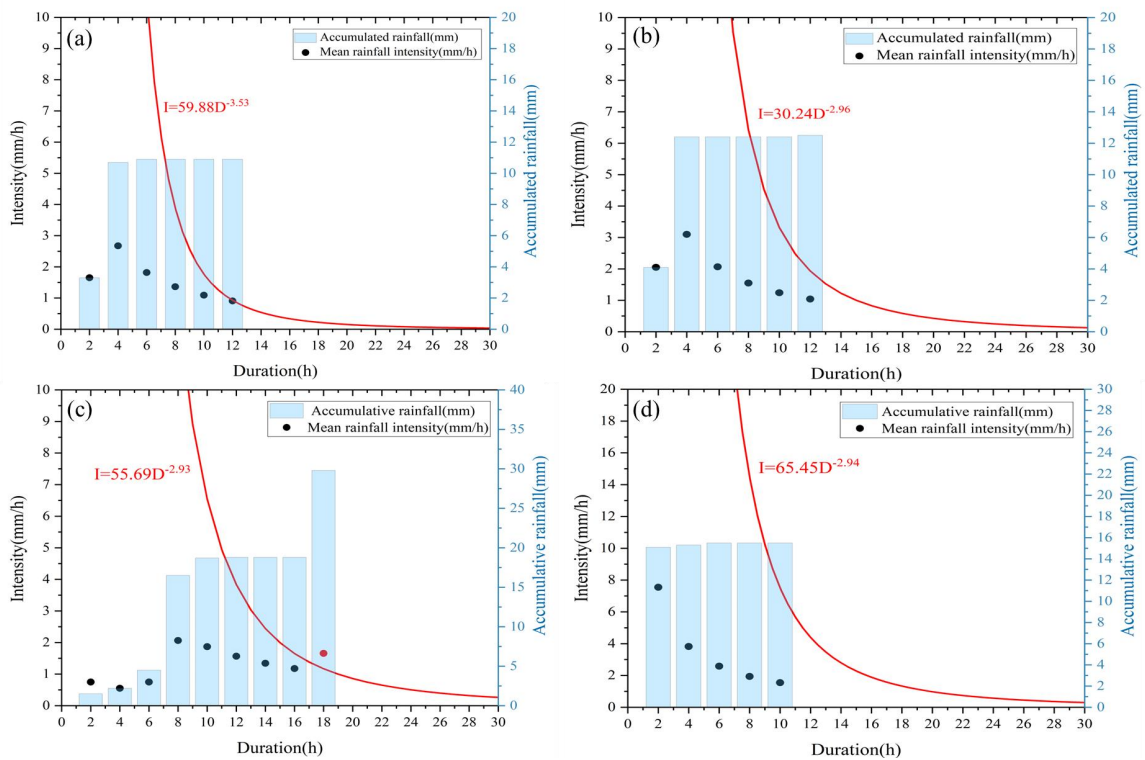
18

1

Table 5 Rainfall process adjustment for HSU with number of 8535

| Time                     | 2:0<br>0 | 4:0<br>0 | 6:0<br>0 | 8:0<br>0 | 10:0<br>0 | 12:0<br>0 | 14:0<br>0 | 16:0<br>0 | 18:0<br>0 | 20:0<br>0 | 22:0<br>0 | 24:0<br>0 |     |
|--------------------------|----------|----------|----------|----------|-----------|-----------|-----------|-----------|-----------|-----------|-----------|-----------|-----|
| Accumulated rainfall(mm) | 0        | 0        | 0        | 0        | 0         | 0.3       | 3.3       | 10.7      | 10.9      | 10.9      | 10.9      | 10.9      |     |
| Before adjustment        | I(mm/h)  | 0        | 0        | 0        | 0         | 0         | 0.2       | 0.7       | 0.6       | 0.5       | 0.5       | 0.5       |     |
|                          | D (h)    | 2        | 4        | 6        | 8         | 10        | 12        | 14        | 16        | 18        | 20        | 22        | 24  |
| After adjustment         | I(mm/h)  | /        |          |          |           |           | 0         | 1.6       | 2.7       | 1.8       | 1.3       | 1.1       | 0.9 |
|                          | D (h)    | /        |          |          |           |           | 0         | 2         | 4         | 6         | 8         | 10        | 12  |

2



3

4 Figure 11 The I-D Curves of HSUs after the adjustment of rainfall process (a. 8535; b. 8561; c. 6066; d.  
5 13108)

### 6 5.3 Comparison with existing approaches in the Fengjie county

7 Statistical methods have been widely used to establish rainfall thresholds for landslides. Liu  
8 (2024) categorized Chongqing into four distinct subregions based on topography, tectonic  
9 structures, lithological stratigraphy, and the distribution and characteristics of landslides, and  
10 established the rainfall thresholds for landslides in each subregion, as shown in Table 6. Fengjie

1 county belongs to Subregion II, with its rainfall threshold is listed in the second row of Table 6. In  
 2 this table, R represents the cumulative daily rainfall, while  $R_e$  signifies the antecedent effective  
 3 rainfall.

4 Table 6 Equations of the thresholds defined for each subregion (Liu et al., 2024)

| Threshold     | 5%                  | 30%                  | 50%                  | 80%                  |
|---------------|---------------------|----------------------|----------------------|----------------------|
| Subregion I   | $R = -1.13R_e + 43$ | $R = -1.13R_e + 70$  | $R = -1.13R_e + 85$  | $R = -1.13R_e + 135$ |
| Subregion II  | $R = -0.93R_e + 38$ | $R = -0.93R_e + 70$  | $R = -0.93R_e + 100$ | $R = -0.93R_e + 145$ |
| Subregion III | $R = -0.96R_e + 40$ | $R = -0.96R_e + 100$ | $R = -0.96R_e + 135$ | $R = -0.96R_e + 180$ |
| Subregion IV  | $R = -1.15R_e + 41$ | $R = -1.15R_e + 76$  | $R = -1.15R_e + 98$  | $R = -1.15R_e + 140$ |

5 The prediction results derived from statistical methods are illustrated in Figure 12, with  
 6 detailed prediction performance parameters provided in Table 7. As depicted in Figure 12, there  
 7 are 5,462 unstable HSUs, primarily located in the northwest and southern mountainous regions.  
 8 According to Table 7, 256 landslide events are successfully predicted by Liu’s model. However,  
 9 the statistical method exhibits a missing alarm rate of 40% and a false alarm rate of 30.4%,  
 10 resulting in low overall precision and accuracy. In contrast, the missing and false alarm rate of the  
 11 HSU\_ID model are 11.8% and 21.1% at the 24<sup>th</sup> hour (Table 1), thus demonstrating superior  
 12 forecasting performance.

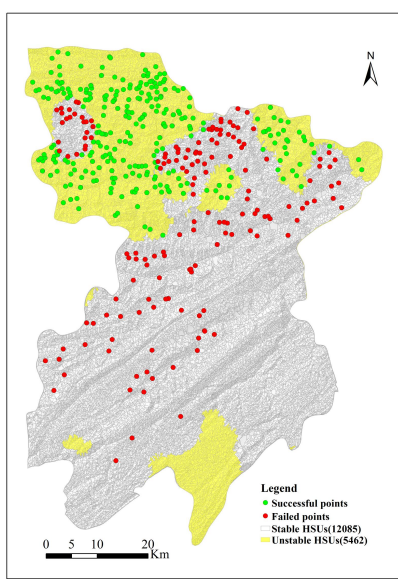


Figure 12 Prediction outcomes generated by Liu’s model

13  
 14  
 15

Table 7 Prediction performance parameters of Liu's model

| Unstable HSUs | TP  | TN    | FP   | FN  | MAR (%) | FPR (%) | Precision(%) | Accuracy(%) |
|---------------|-----|-------|------|-----|---------|---------|--------------|-------------|
| 5462          | 256 | 11915 | 5206 | 170 | 40.0    | 30.4    | 66.4         | 69.4        |

#### 5.4 Limitations and future work

The method proposed in this paper reduces dependence on landslide inventory data and avoids the issue of excessive computation time associated with physical models. This offers promising application prospects for emergency early warning in regions of third-world countries where landslide inventory data are scarce. However, it should be noted that the calculation of  $HSU_{prob}$  relies on regional-scale mechanical parameters. Therefore, establishing the distribution of mechanical parameters in Southwest China through field sampling, experiments, and spatial analysis is an important task for the future. Another important task lies in optimizing the model algorithm, because the physical mechanisms of rainfall landslides are extremely complex, and the soil-water coupling process under rainfall involves significant nonlinearity (Apip et al., 2010). Some machine learning methods that incorporate physical frameworks are expected to accurately describe this issue (for example the PINN) . Therefore, improving the model algorithm by combining machine learning with physical approaches is another important task for the future.

#### 6 Conclusion

Currently, the operational forecasting of rainfall-induced landslides over regional scales of thousands of square kilometers faces significant challenges. Conventional physical and statistical approaches have shown limitations in terms of achieving satisfactory results. This study utilized HSU as a basis to integrate physical models and rainfall threshold methods for a warning model applicable to large-scale regions. The warning model employs HSU as a prediction unit to improve the clarity of the warning results, physical methods are utilized to develop the warning criteria, thereby reducing the overreliance on historical observational data, and a database of rainfall parameters across different rainfall scenarios is constructed, which enhances the efficiency and applicability of the warning model. The prediction performance was validated through a case study of “8.31” rainfall landslides in Fengjie County. The conclusions are as follows.

(1) A rainfall-triggered landslide warning model was established by integrating HSUs, physical approaches, and rainfall parameters. Initially, a grid-based HSU hydrological analysis technique was established to determine the soil moisture content distribution within the HSUs

1 during different rainfall hours. Subsequently, computer graphics algorithms, random search  
2 techniques, and infinite slope models were used to develop a regional-scale HSU stability analysis  
3 method. Soil mechanics parameters at the limit of water content and probability density functions  
4 were used to describe the spatial uncertainty of the soil mechanical parameters within the HSU  
5 during rainfall infiltration, allowing for the calculation of the instability probability of the  
6 HSU. Different rainfall scenarios were simulated to derive rainfall intensity  $I$  and duration  $D$  data  
7 that can trigger HSU instability, thereby constructing early warning curves for the rainfall  
8 thresholds of the HSU.

9 (2) A database for the I-D curve fitting parameters  $\alpha$  and  $\beta$  across various AER levels was  
10 established. This database includes  $\alpha$  and  $\beta$  data for 17,547 HSUs across 20 AER levels,  
11 amounting to a total of 350,940 records, thus offering substantial data support for rainfall-induced  
12 landslide predictions in Fengjie County. In practical applications, it is sufficient to quickly issue  
13 warning information by assessing the relationship between the values of  $I$  and  $\alpha D^\beta$ , thereby  
14 reducing the time required to calculate the safety factors using conventional physical models. The  
15 calculation efficiency test indicates that the warning mode can perform forecasts for thousands of  
16 kilometers within a runtime of less than 12 min, thereby meeting the operational needs for  
17 real-time warnings over large regional scales.

18 (3) The case study indicates that the distribution trends of unstable HSUs align well with  
19 rainfall characteristics. As the rainfall duration increased, the missing alarm rate (MAR) gradually  
20 decreased, while the false alarm rate (FAR) continued to increase. Taking the 24-hour forecast  
21 results as an example, the missing alarm rate was 11.8%, while the false alarm rate was 21.1%.  
22 ROC analysis revealed that the accuracy of the forecast result at this moment was 80.7%, with a  
23 precision of 79.1%, reflecting satisfactory overall forecasting performance. Further discussion of  
24 the false alarm rate suggests that adjusting the spatial locations of rainfall intensity and duration  
25 data points based on the rainfall characteristics of each HSU may be conducive to reducing false  
26 alarm rates.

27  
28  
29  
30  
31 **Acknowledgements**

1 The authors would like to acknowledge the Chongqing Meteorological Bureau, China for  
2 providing the QPE and QPF data free of charge. We are also thankful to the Land and Resources  
3 Bureau of Fengjie county for their support with the field investigation.

## 6 **Conflict of Interest Statement**

7 All authors declare that they have no conflicts of interest. We declare that we do not have any  
8 commercial or associative interests that represent a conflict of interest in connection with the  
9 submitted work.

## 11 **Author contributions**

12 **KW:** Conceptualization, Writing – original draft, Supervision, Data curation Funding acquisition;  
13 **LX:** Supervision, Visualization, Writing – original draft; **SX:** Investigation, Data curation,  
14 Validation; **SZ:** Methodology, Resources, Validation; **YJ:** Supervision, Validation, Software; **JZ:**  
15 Investigation, Software; **HG:** Investigation, Visualization; **LZ:** Project administration,  
16 Visualization; **ZW:** Project administration, Writing – review & editing; **FQ:** Writing – review &  
17 editing.

## 19 **Disclosure statement**

20 No potential conflict of interest was reported by the author(s).

## 22 **Funding**

23 This work was supported by the [National Natural Science Foundation of China] under Grant  
24 [42301083]; and the Training Program for Young Backbone Teachers in Higher Education  
25 Institutions of Henan Province[2025GGJS094]; and [General Project of Henan Province  
26 Education Science Planning, China] under Grant [2025YB0116].

## 28 **Data availability statement**

29 The datasets supporting this study are available from the corresponding author upon reasonable  
30 request.

## 33 **Reference**

- 34 Alvioli, M., Guzzetti, F., & Marchesini, I. 2020. Parameter-free delineation of slope units and t  
35 errain subdivision of Italy. *Geomorphology*, 358, 107124. <https://doi.org/10.1016/j.geomorph.2020.107124>.
- 37 Aristizábal, E., Vélez, J. I., Martínez, H. E., & Jaboyedoff, M. 2016. SHIA\_Landslide: a distri  
38 buted conceptual and physically based model to forecast the temporal and spatial occur  
39 rence of shallow landslides triggered by rainfall in tropical and mountainous basins. *La  
40 ndslides*, 13(3), 497-517. <https://doi.org/10.1007/s10346-015-0580-7>.
- 41 ASTM D6528-17. (2017). Standard test method for consolidated undrained direct simple shear t  
42 esting of fine grain soils. ASTM International: West Conshohocken, PA, USA
- 43 Apip, Takara K, Yamashiki Y, Sassa K, Bagiawan Ibrahim A, and Fukuoka H, 2010. A distributed  
44 hydrological-geotechnical model using satellite-derived rainfall estimates for shallow landslide

- 1 prediction system at a catchment scale, *Landslides*, 7: 237–258.
- 2 Baum, R. L., Savage, W. Z., & Godt, J. 2008. TRIGRS—a Fortran program for transient rainf  
3 all infiltration and grid-based regional slope-stability analysis. US Geological Survey O  
4 pen File Report 2008-1159, 2.
- 5 Bezak, N., Šraj, M., & Matjaž, M. 2016. Copula-based IDF curves and empirical rainfall thres  
6 holds for flash floods and rainfall-induced landslides. *Journal of Hydrology*, 541, 272-2  
7 84. <https://doi.org/10.1016/j.jhydrol.2016.02.058>.
- 8 Bogaard, T., & Greco, R. 2018. Invited perspectives: Hydrological perspectives on precipitation  
9 intensity-duration thresholds for landslide initiation: proposing hydro-meteorological thr  
10 esholds. *Natural Hazards and Earth System Sciences*, 18, 31-39. [https://doi.org/10.5194/  
11 nhess-18-31-2018](https://doi.org/10.5194/nhess-18-31-2018).
- 12 Brunetti, M., Peruccacci, S., Rossi, M., S, L., Valigi, D., & Guzzetti, F. 2010. Rainfall threshol  
13 ds for the possible occurrence of landslides in Italy. *Natural Hazards and Earth System  
14 Sciences*, 10. <https://doi.org/10.5194/nhess-10-447-2010>.
- 15 Cuomo, S., Di Perna, A., & Martinelli, M. 2021. Modelling the spatio-temporal evolution of a  
16 rainfall-induced retrogressive landslide in an unsaturated slope. *Engineering Geology*, 2  
17 94, 106371. <https://doi.org/10.1016/j.enggeo.2021.106371>.
- 18 Domènech, G., Alvioli, M., & Corominas, J. 2019. Preparing first-time slope failures hazard m  
19 aps: from pixel-based to slope unit-based. *Landslides*, 17, 249-265. [https://doi.org/10.10  
20 07/s10346-019-01279-4](https://doi.org/10.1007/s10346-019-01279-4).
- 21 Fawcett, T. 2006. Introduction to ROC analysis. *Pattern Recognition Letters*, 27, 861-874. [https:  
22 //doi.org/10.1016/j.patrec.2005.10.010](https://doi.org/10.1016/j.patrec.2005.10.010).
- 23 Greco, V. 1996. Efficient Monte Carlo Technique for Locating Critical Slip Surface. *Journal of  
24 Geotechnical Engineering*, 122, 517-525. [https://doi.org/10.1061/\(ASCE\)0733-9410\(1996\)  
25 122:7\(517\)](https://doi.org/10.1061/(ASCE)0733-9410(1996)122:7(517)).
- 26 Gu, T., Wang, J., Fu, X., & Liu, Y. 2014. GIS and limit equilibrium in the assessment of regi  
27 onal slope stability and mapping of landslide susceptibility. *Bulletin of Engineering Ge  
28 ology and the Environment*, 74, 1-11. <https://doi.org/10.1007/s10064-014-0689-2>.
- 29 Guo, Z., Torra, O., Hürlimann, M., Abancó, C., & Medina, V. 2022. FSLAM: A QGIS plugin  
30 for fast regional susceptibility assessment of rainfall-induced landslides. *Environmental  
31 Modelling & Software*, 150, 105354. <https://doi.org/10.1016/j.envsoft.2022.105354>.
- 32 He, X., Hong, Y., Vergara, H., Kirstetter, P.-E., Gourley, J., Zhang, Y., Qiao, G., & Liu, C. 20  
33 16. Development of a Coupled Hydrological-geotechnical Framework for Rainfall-induc  
34 ed Landslides Prediction. *Journal of Hydrology*, 543. [https://doi.org/10.1016/j.jhydrol.201  
35 6.10.016](https://doi.org/10.1016/j.jhydrol.2016.10.016).
- 36 Hong, M., Kim, J., & Jeong, S. 2017. Rainfall intensity-duration thresholds for landslide predic  
37 tion in South Korea by considering the effects of antecedent rainfall. *Landslides*, 15. [h  
38 ttps://doi.org/10.1007/s10346-017-0892-x](https://doi.org/10.1007/s10346-017-0892-x).
- 39 Hong, Y., Hiura, H., Shino, K., Sassa, K., Suemine, A., Fukuoka, H., & Wang, G. 2005. The i  
40 nfluence of intense rainfall on the activity of large-scale crystalline schist landslides in  
41 Shikoku Island, Japan. *Landslides*, 2, 97-105. [https://doi.org/10.1007/s10346-004-0043-z  
42 .](https://doi.org/10.1007/s10346-004-0043-z)
- 43 Huang, F., Tao, S., Chang, Z., Huang, J., Fan, X., Jiang, S.-H., & Li, W. 2021. Efficient and  
44 automatic extraction of slope units based on multi-scale segmentation method for lands

- lide assessments. *Landslides*, 18. <https://doi.org/10.1007/s10346-021-01756-9>.
- Kanungo, D., & Sharma, S. 2014. Rainfall thresholds for prediction of shallow landslides around Chamoli-Joshimath region, Garhwal Himalayas, India. *Landslides*, 11, 629-638. <https://doi.org/10.1007/s10346-013-0438-9>.
- Kim, S., Chun, K., Kim, M., Catani, F., Choi, B., & Seo, J. I. 2020. Effect of antecedent rainfall conditions and their variations on shallow landslide-triggering rainfall thresholds in South Korea. *Landslides*, 18. <https://doi.org/10.1007/s10346-020-01505-4>.
- Liang, W.-L., & Uchida, T. 2021. Performance and topographic preferences of dynamic and steady models for shallow landslide prediction in a small catchment. *Landslides*, 19. <https://doi.org/10.1007/s10346-021-01771-w>.
- Li, D., Wang, Z., Guo, H., Zhang, Y., Cheng, X., & Yu, Q. 2025. Deep Learning in Slope Stability Analysis: Evolution, Challenges, and Future Directions. *Geotechnical and Geological Engineering*, 43(8), 1-48.
- Liu SH, Du J, Yin KL, Zhou C, Huang CC, Jiang J, Yu J, 2024. Regional early warning model for rainfall induced landslide based on slope unit in Chongqing, China. *Engineering Geology*, 333: 107464.
- Ma, T., Changjiang, L., Lu, Z., & Bao, Q. 2015. Rainfall intensity–duration thresholds for the initiation of landslides in Zhejiang Province, China. *Geomorphology*, 245. <https://doi.org/10.1016/j.geomorph.2015.05.016>.
- Marra, F. 2018. Rainfall thresholds for landslide occurrence: systematic underestimation using coarse temporal resolution data. *Natural Hazards*, 95. <https://doi.org/10.1007/s11069-018-3508-4>.
- Medina, V., Hürlimann, M., Guo, Z., Lloret, A., & Vaunat, J. 2021. Fast physically-based model for rainfall-induced landslide susceptibility assessment at regional scale. *CATENA*, 201, 105213. <https://doi.org/10.1016/j.catena.2021.105213>.
- Montgomery, D., & Dietrich, W. 1994. A Physically Based Model for the Topographic Control on Shallow Landsliding. *Water Resources Research - WATER RESOUR RES*, 30, 1153-1172. <https://doi.org/10.1029/93WR02979>.
- Montrasio, L., & Valentino, R. 2016. Modelling Rainfall-induced Shallow Landslides at Different Scales Using SLIP - Part I. *Procedia Engineering*, 158, 476-481. <https://doi.org/10.1016/j.proeng.2016.08.475>.
- Moeineddin, A., Seguí, C., Dueber, S., & Fuentes, R. 2023. Physics-informed neural networks applied to catastrophic creeping landslides. *Landslides*, 20(9), 1853-1863.
- Pinho, T., & Augusto Filho, O. 2022. Landslide susceptibility mapping using the infinite slope, SHALSTAB, SINMAP, and TRIGRS models in Serra do Mar, Brazil. *Journal of Mountain Science*, 19, 1018-1036. <https://doi.org/10.1007/s11629-021-7057-z>.
- Pradhan, A., Lee, S.-R., Kim, Y.-T. 2018. A shallow slide prediction model combining rainfall threshold warnings and shallow slide susceptibility in Busan, Korea. *Landslides*, 16: 647-659. doi: <https://doi.org/10.1007/s10346-018-1112-z>
- Rigon, R., Bertoldi, G., & Over, T. 2006. GEOTop: A Distributed Hydrological Model with Coupled Water and Energy Budgets. *Journal of Hydrometeorology*, 7, 2006. <https://doi.org/10.1175/JHM497.1>.
- Rosi, A., Segoni, S., Canavesi, V., Monni, A., Gallucci, A., & Casagli, N. 2020. Definition of 3D rainfall thresholds to increase operative landslide early warning system performance

1 s. Landslides, 18. <https://doi.org/10.1007/s10346-020-01523-2>.

2 Rossi, G., Catani, F., Leoni, L., Segoni, S., & Tofani, V. 2013. HIRESSES: a physically based s  
3 lope stability simulator for HPC applications. *Nat. Hazards Earth Syst. Sci.*, 13(1), 151  
4 -166. <https://doi.org/10.5194/nhess-13-151-2013>.

5 Tarboton, D., & Goodwin, C. 1970. The SINMAP approach to terrain stability mapping.

6 Tufano, R., Formetta, G., Calcaterra, D., & De Vita, P. 2021. Hydrological control of soil thic  
7 kness spatial variability on the initiation of rainfall-induced shallow landslides using a  
8 three-dimensional model. *Landslides*, 18. <https://doi.org/10.1007/s10346-021-01681-x>.

9 Turel, M., & Frost, J. (2011). *Delineation of Slope Profiles from Digital Elevation Models for*  
10 *Landslide Hazard Analysis*. [https://doi.org/10.1061/41183\(418\)87](https://doi.org/10.1061/41183(418)87)

11 Van Genuchten, M. 1980. A Closed-form Equation for Predicting the Hydraulic Conductivity of  
12 Unsaturated Soils<sup>1</sup>. *Soil Science Society of America Journal*, 44. <https://doi.org/10.2136/sssaj1980.03615995004400050002x>.

13 Wang, K., Xie, S., Zhang, S., Zhu, L., Ma, J., Liu, D., & Yang, H. 2024. Creating a big data  
14 source of landslide deformation stages: New thoughts on identifying displacement war  
15 ning thresholds. *Journal of Asian Earth Sciences*, 266, 106120. <https://doi.org/10.1016/j.jseacs.2024.106120>.

16 Wang, K., & Zhang, S. 2021. Rainfall-induced landslides assessment in the Fengjie County, Th  
17 ree-Gorge reservoir area, China. *Natural Hazards*, 108, 1-28. <https://doi.org/10.1007/s11069-021-04691-z>.

18 Wang, K., Zhang, S., & Wei, F. 2019. Geotechnical mechanical parameters determination of pr  
19 ediction unit based spatial interpolation technique. *JOURNAL OF NATURAL DISAS  
20 TERS*, 28, 209-219. <https://doi.org/10.13577/j.jnd.2019.0523>.

21 Wang, K., Zhang, S., Xie, W.-l., & Guan, H. 2023. Prediction of the instability probability for  
22 rainfall induced landslides: the effect of morphological differences in geomorphology  
23 within mapping units. *Journal of Mountain Science*, 20, 1249-1265. <https://doi.org/10.1007/s11629-022-7789-4>.

24 Wang, X., Zhang, L., Wang, S., & Lari, S. 2013. Regional landslide susceptibility zoning with  
25 considering the aggregation of landslide points and the weights of factors. *Landslides*,  
26 11. <https://doi.org/10.1007/s10346-013-0392-6>.

27 Yan, G., Cheng, H., Jiang, Z., Teng, L., Tang, M., Shi, T., Jiang, Y., Yang, G., & Zhou, Q. 2  
28 021. Recognition of Fluvial Bank Erosion Along the Main Stream of the Yangtze Rive  
29 r. *Engineering*, 19. <https://doi.org/10.1016/j.eng.2021.03.027>.

30 Zhang LY, Zhang JM (2006) Extended algorithm using Monte Carlo techniques for searching g  
31 eneral critical slip surface in slope stability analysis. *Yantu Gongcheng Xuebao Chin J*  
32 *Geotech Eng* 28(7):857–862 (in Chinese)

33 Zhang, S., Ma, Z., Li, Y., Hu, K., Zhang, Q., & Li, L. 2021. A grid-based physical model to  
34 analyze the stability of slope unit. *Geomorphology*, 391, 107887. <https://doi.org/10.1016/j.geomorph.2021.107887>.

35 Zhang, S., Xu, C. X., Wei, F., Hu, K., Xu, H., Zhao, L. Q., & Zhang, G. P. 2019. A physics-  
36 based model to derive rainfall intensity-duration threshold for debris flow. *Geomorphol  
37 ogy*, 351, 106930. <https://doi.org/10.1016/j.geomorph.2019.106930>.

38 Zhang, S., Zhao, L., Delgado Tellez, R., & Bao, H. 2018. A physics-based probabilistic forecas  
39 ting model for rainfall-induced shallow landslides at regional scale. *Natural Hazards an*

1 d Earth System Sciences, 18, 969-982. <https://doi.org/10.5194/nhess-18-969-2018>.

2 Zhuang, J., Iqbal, J., Jianbing, P., & Tieming, L. 2014. Probability Prediction Model for Landsl  
3 ide Occurrences in Xi'an, Shaanxi Province, China. Journal of Mountain Science, 11, 3  
4 45-359. <https://doi.org/10.1007/s11629-013-2809-z>.

5 Zhuang, J., Peng, J., Xu, Y., Xu, Q., Zhu, X., & Li, W. E. I. 2016. Assessment and mapping  
6 of slope stability based on slope units: A case study in Yan'an, China. Journal of Earth  
7 System Science, 125. <https://doi.org/10.1007/s12040-016-0741-7>.